

# A Hollow Porous Metal-Organic Framework Enabled Polyethylene Oxide Based Composite Polymer Electrolytes for All-Solid-State Lithium Batteries

Yubing Hu,<sup>[a]</sup> Tianshi Feng,<sup>[a]</sup> Lei Xu,<sup>[a]</sup> Lifeng Zhang,<sup>\*[a]</sup> and Langli Luo<sup>\*[a]</sup>

Composite polymer electrolytes (CPEs) are replacing traditional liquid electrolytes for next-generation all-solid-state batteries (ASSBs) with enhanced safety and uncompromising electrochemical properties. However, short-circuit due to lithium-dendrite growth in the CPEs largely hinders its practical applications. Here, we report a thin CPE composed of the hollow ZIF-8 encapsulating Li-ionic liquids (ZIF-8/IL) nano-filters and polyethylene oxide (PEO) matrix. It shows an ionic conductivity of  $1.41 \times 10^{-4} \text{ S cm}^{-1}$  at 25 °C with improved surface

roughness, thermal stability, and electrochemical stability. The specific core-shell structure of fillers benefits from its insulation shell for inhibiting lithium dendrite growth and the inner cavity for storing sufficient Li-IL with enhanced Li diffusivity. The CPE with 30% filler (30 H-Z CPE) content exhibits excellent cycle stability of 770 h in the Li symmetric cell and an outstanding discharge capacity of 182.5 mAh g<sup>-1</sup> and capacity retention of 73% after 100 cycles at 0.1 C and 60 °C in the Li/30 H-Z CPE/NCM811 asymmetric cell.

## Introduction

Lithium-ion batteries (LIBs) have numerous applications in electric vehicles and portable electronic devices due to their high energy density and long-term cycle stability.<sup>[1–4]</sup> As the mainstream electrolyte at present, the flammable liquid electrolyte still has a series of safety issues for automobile applications,<sup>[5–8]</sup> hence, safe and reliable solid electrolytes enabled all-solid-state batteries (ASSBs) have attracted prevailing attention in both scientific and industrial sectors.<sup>[9–12]</sup> Among them, the practical application of ceramic solid electrolytes with high conductivity is hindered by their brittleness and poor interfacial contact with the electrode materials.<sup>[13]</sup> The flexible polymer electrolytes have been successfully used in Li-polymer batteries and exhibit potentials to circumvent the above mechanical and interfacial problems of ceramic electrolytes, but their low intrinsic ionic conductivity and poor cyclability limit the further application of polymer electrolytes.<sup>[14–18]</sup> Therefore, it is urgent to develop electrolytes with both excellent conductivity and benign interface compatibility.

Composite polymer electrolytes (CPEs) which combine the advantages of inorganic ceramic electrolytes and organic polymer electrolytes are the hotspot of current research for ASSBs.<sup>[19–25]</sup> The CPEs prepared using polymers such as PEO as the matrix and inorganic fillers with high ion-conductivity can effectively improve Li<sup>+</sup> transport, interface wettability, thermal

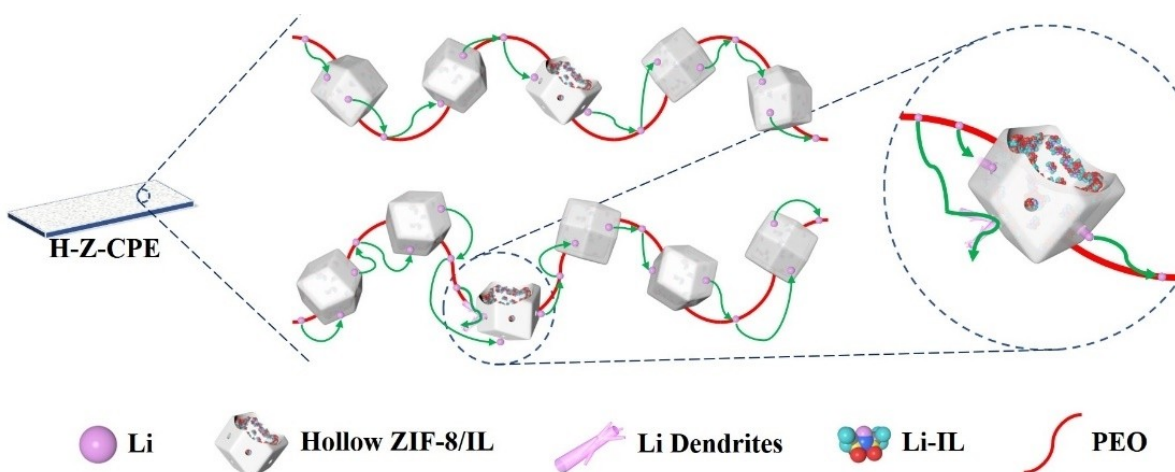
stability, and mechanical stability through the combination of organic and inorganic materials.<sup>[26–28]</sup> However, batteries assembled with CPEs are prone to have lithium-dendrite growth in the polymer matrix as well as at the grain boundaries of inorganic ceramic electrolyte fillers upon long-term cycling, resulting in short-circuit/failure of the batteries.<sup>[29–31]</sup> Thus, it is necessary to develop a special filler for inhibiting lithium dendrite to improve the cycle stability of batteries.

Metal-organic framework (MOF) is extensively applied in the field of gas separation, catalysis, heavy metal ions absorption, oil/water separation, drug delivery, membrane synthesis, and electrochemistry due to its unique porous structure, large specific surface area, and excellent thermal stability.<sup>[32–39]</sup> MOF formed by center metal ion clusters and organic ligands is a natural solid-state electrolyte due to its intrinsically poor electrical conductivity with adjustable ion transport capability.<sup>[40,41]</sup> The pore structure of MOF can adsorb the Li-IL to form a quasi-solid electrolyte filler with high ionic conductivity. Meanwhile, the insulating nature of MOF can effectively restrain the growth of lithium dendrite. However, the use of MOF in the field of solid electrolytes is rarely reported.

In this work, we start with the ZIF-8 as an insulating and Li<sup>+</sup> ion transporting scaffold due to its micro-channeled structure and employ an acid etching method to create a hollow structure to accommodate Li-containing ILs with the expectation of boosting the Li<sup>+</sup> conductivity and maintaining a stable long-term cyclability, as shown in Scheme 1. Etching not only greatly improves the pore volume of ZIF-8, but also significantly widens the pore size, thereby facilitating the passage and storage of more Li-IL, forming a quasi-solid-state electrolyte filler with a core-shell structure. The slender CPEs ( $\approx 50 \mu\text{m}$ ) prepared using novel hollow ZIF-8/IL filler with a core-shell structure by tape casting method enhance the ionic conductivity, interface resistance, stability of LiF layer and thermal/

[a] Y. Hu, T. Feng, L. Xu, Dr. L. Zhang, Prof. L. Luo  
Institute of Molecular Plus  
Tianjin University  
300072 Tianjin, China  
E-mail: lfzhang007@tju.edu.cn  
luolangli@tju.edu.cn

 Supporting information for this article is available on the WWW under  
<https://doi.org/10.1002/batt.202100303>



Scheme 1. Schematic illustration of structure of the hollow ZIF-8/IL filler and its function as storage room for LiTFSI.

electrochemical stability by tuning the surface roughness, dispersion of fillers, which enable great electrochemical performance in both symmetric Li cells and full cells.

## Results and Discussions

### Morphology and pore structure of hollow ZIF-8/IL fillers

First, we synthesize ZIF-8 with a distinct rhomboid dodecahedron shape and a size of around 200 nm, as shown in the scanning electron microscopy (SEM) images of Figure 1(a and b). On its basis, hollow ZIF-8 particles were successfully fabricated by etching with the tannic acid without changing their original morphology, as shown in Figure 1(c and d). In addition, the hollow ZIF-8 appears as the gray-purple color and

bulk blocks, macroscopically (Figure 1m). The scanning transmission electron microscopy high-angle annular dark-field (STEM-HAADF) images in Figure 1(e and h) show the etched hollow ZIF-8 and ZIF-8 infused with ionic liquids with Li salt (Li-IL). The energy-dispersive spectrum (EDS) mapping of the characteristic elemental distribution verifies the encapsulation Li-IL was infused into the cavity of hollow ZIF-8. The Zn and N elemental belonging to the ZIF-8 precursor were uniformly distributed in both hollow ZIF-8 and the shell layer of hollow ZIF-8/IL, as shown in Figure 1(f and j). The F and S elemental belonging to Li-IL were distributed throughout the shell and core layers of hollow ZIF-8/IL (Figure 1 i–l), which confirms Li-IL was favorably transfused in the cavity of the hollow ZIF-8.

Table 1 shows that compared with ZIF-8, hollow ZIF-8 possesses a larger pore size of 9.535 nm (1.061 nm for ZIF-8) and a larger pore volume of  $1.063 \text{ cm}^3 \text{ g}^{-1}$  ( $0.674 \text{ cm}^3 \text{ g}^{-1}$  for

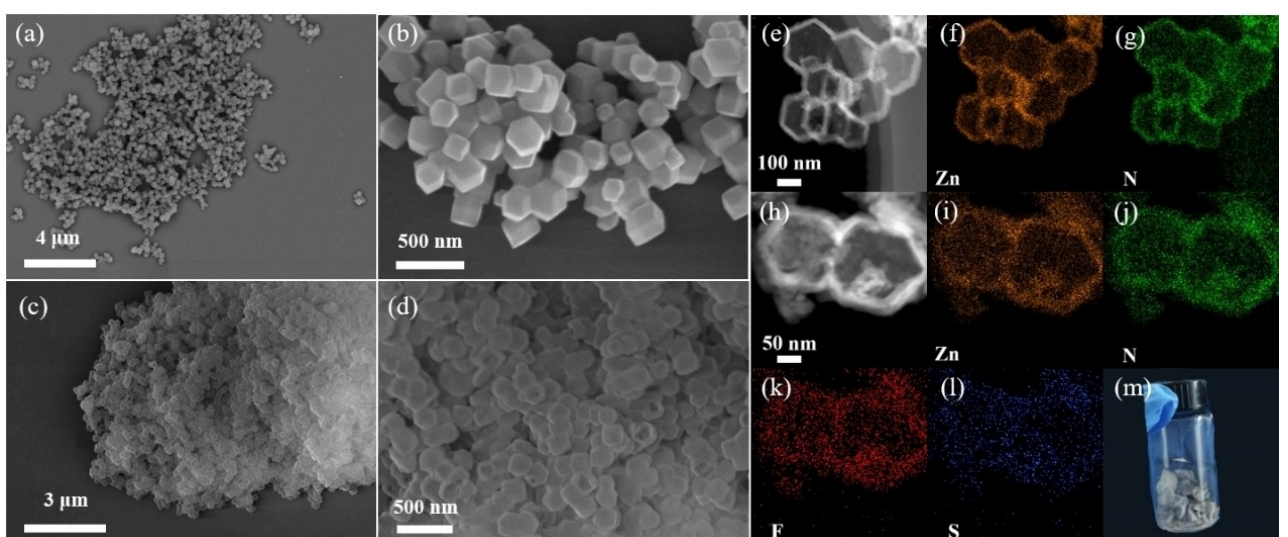


Figure 1. Field-emission (FE)SEM images of a) and b) ZIF-8, c) and d) Hollow ZIF-8. STEM-HAADF images of e) Hollow ZIF-8 and h) Hollow ZIF-8/IL. EDS elemental mappings of f) and i) Zn, g) and j) N, k) F, and l) S. Photograph of m) Hollow ZIF-8.

Materials	Pore diameter/[nm]	Pore volume/[cm <sup>3</sup> g <sup>-1</sup> ]
ZIF-8	1.061	0.674
Hollow ZIF-8	9.535	1.063

ZIF-8). The hollow ZIF-8 facilitates the transmission of Li<sup>+</sup> (0.076 nm) and entry of TFSI<sup>-</sup> (0.76 nm) and EMIM<sup>+</sup> (0.79 nm) and provides a greater volume of Li-IL perfusion. Finally, novel hollow ZIF-8/IL quasi-solid electrolyte filler was obtained through encapsulating Li-IL into the cavity of the core layer and pore of the shell layer.

### Li-conductivity of the CPEs

The namely x H-Z-CPEs (x stands for the weight percent of fillers) were fabricated by tape casting method which greatly reduced the film thickness and saved the cost by homogeneous mixing PEO, LiTFSI, and different mass of hollow ZIF-8/IL fillers in anhydrous acetonitrile. At the same time, PEO CPE was also prepared as a control sample by the same method without adding hollow ZIF-8/IL fillers. First, the ionic conductivities of CPEs were measured using electrochemical impedance spectroscopy (EIS) to analyze the effect of the hollow ZIF-8/IL fillers and determine the optimal filler mass in CPEs. As shown in Figure 2(a), PEO CPE with a bulk resistance of 404.2 Ω has an ionic conductivity of  $4.31 \times 10^{-6}$  S cm<sup>-1</sup> at room temperature. Compared with the PEO CPE, the bulk resistance of the x H-Z-CPE drastically decreased with the increasing filler mass.

Specifically, 30 H-Z-CPE with a resistance of 34.9 Ω possesses an ionic conductivity of  $1.41 \times 10^{-4}$  S cm<sup>-1</sup> while the ionic conductivity of 40 H-Z-CPE has a trivial increase, which indicates 30% is optimal filler content. A moderate amount of hollow ZIF-8/IL fillers improves the ionic conductivity of the CPEs by accelerating the Li<sup>+</sup> transmission.<sup>[42,43]</sup> Besides, this novel hollow ZIF-8/IL effectively suppresses the crystallization of the PEO matrix, thus beneficial to the Li<sup>+</sup> movement in the amorphous area. As shown in Figure 2(b), X-ray diffraction (XRD) was used to analyze the crystallinity of the CPEs. Compared to the ZIF-8 crystal structure reported in the literature, no other diffraction peak was detected in hollow ZIF-8/IL filler, which indicated the interaction between hollow ZIF-8 and Li-IL was simple physical adsorption.<sup>[44]</sup> For the PEO CPE, two obvious diffraction peaks around 19.5° and 23.6° were ascribed to the PEO with a high degree of crystallinity, which delays ion transport along the polymer chains.<sup>[45,46]</sup> With the increasing amount of hollow ZIF-8/IL filler added, these two sharp characteristic diffraction peaks belonging to highly crystalline PEO gradually weakened until completely disappeared when the filler mass reached 30%, which indicated 30 H-Z-CPE had a quasi-amorphous structure. This result supports the observed Li<sup>+</sup> conductivity increase in Figure 2(a), which indicates hollow ZIF-8/IL filler could accelerate the transformation of CPEs from the crystal state to the amorphous state.

Furthermore, the differential scanning calorimeter (DSC) curves of the PEO CPE and 30 H-Z-CPE illustrate the effect of the hollow ZIF-8/IL filler on the phase transition behaviors of CPEs. Figure 2(c) shows the glass transition temperature ( $T_g$ ) for 30 H-Z-CPE of -51.0 °C is distinctly lower than that of PEO CPE

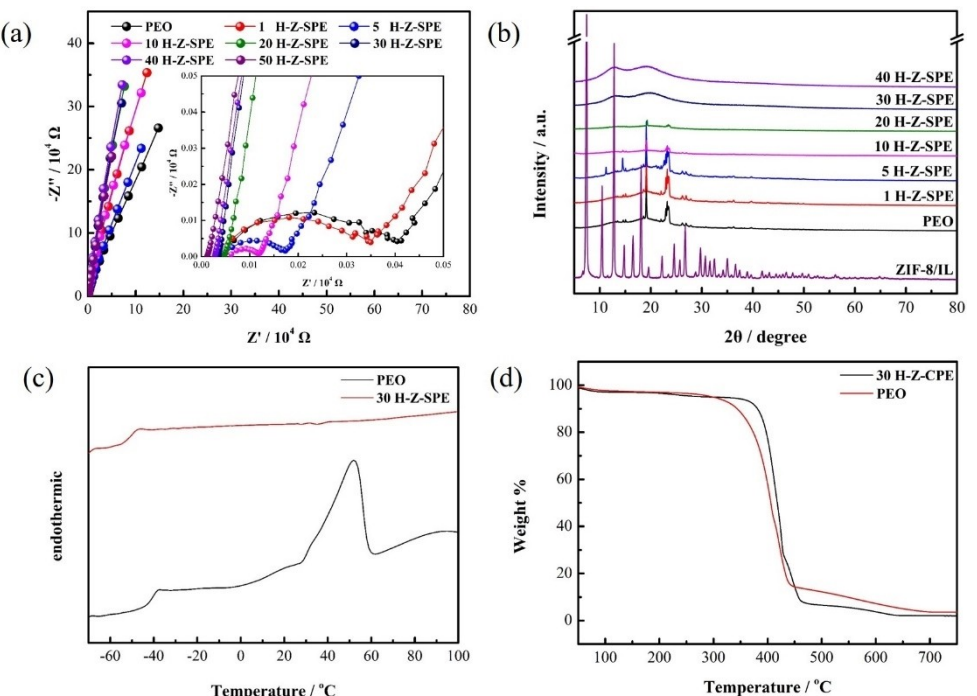
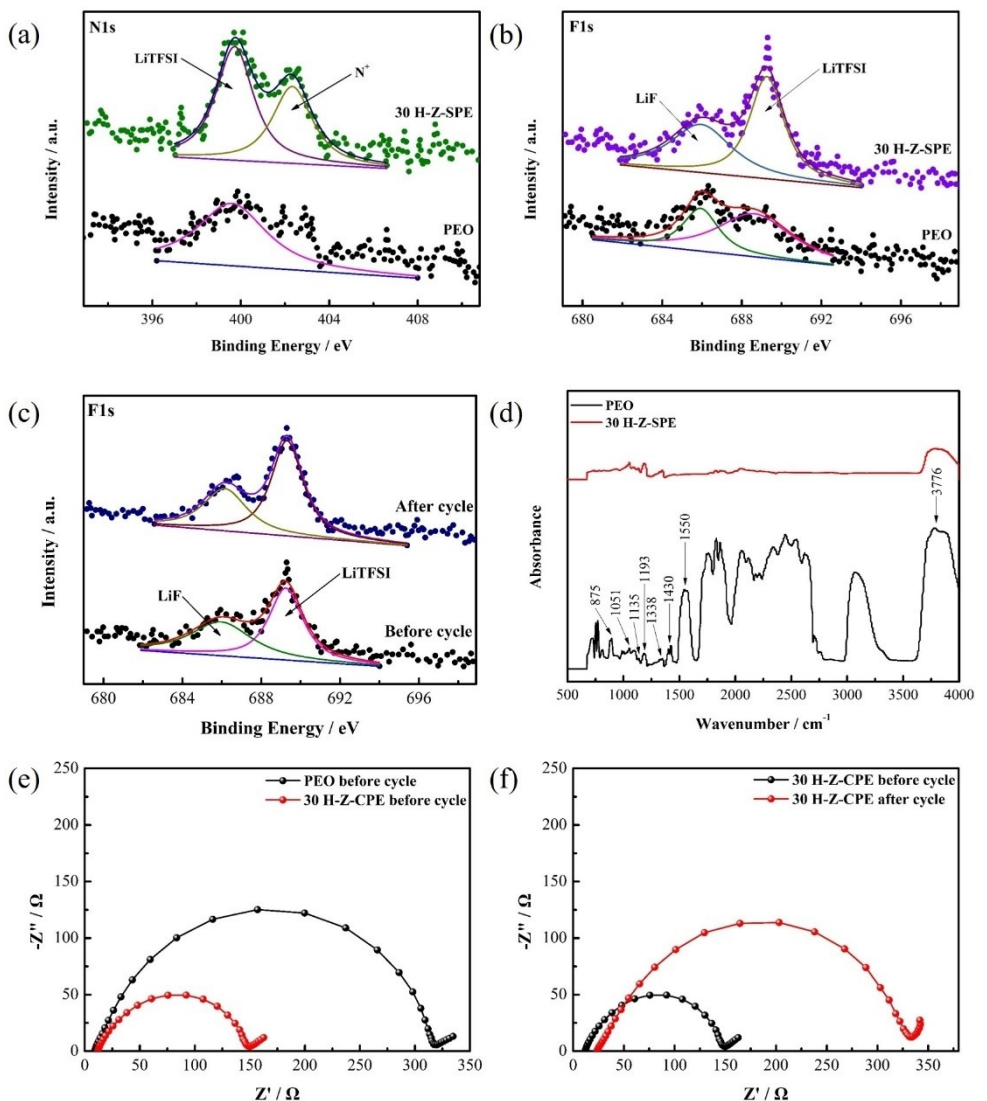


Figure 2. a) Nyquist plots of PEO CPE and x-H-Z-CPE at room temperature. b) XRD patterns of ZIF-8/IL, PEO CPE and x-H-Z-CPE. c) DSC curves of PEO CPE and 30 H-Z-CPE. d) TG curves of PEO CPE and 30 H-Z-CPE.

of  $-41.4^{\circ}\text{C}$  in the temperature rise zone, indicating that the crystallinity of 30 H-Z-CPE is much lower than that of the PEO CPE. Therefore, 30 H-Z-CPE with low crystallinity was beneficial to the transformation of  $\text{Li}^+$  thus possessed the optimal ionic conductivity.<sup>[47]</sup> In addition, the melting point ( $T_m$ ) of PEO CPE was  $51.9^{\circ}\text{C}$  corresponding to high melting enthalpy, which also indicated high crystallinity of PEO inhibited the ion transport in the polymer chains.<sup>[48,49]</sup> Besides, TGA was used to determine the safe operating temperature range of the CPEs. Figure 2(d) shows distinct mass loss corresponding to the decomposition of the polymer matrices of the 30 H-Z-CPE at  $400^{\circ}\text{C}$  and the PEO CPE at  $300^{\circ}\text{C}$ , indicating that hollow ZIF-8/IL filler effectively increases the thermal stability of the CPEs. The interaction between IL and hollow ZIF-8 lead to the fluorination of the IL anion, which was the main reason for the increased thermal stability limit of the CPEs.<sup>[50]</sup>

### Interfacial properties of CPE thin films

Although the CPE thin film possessed a high ionic conductivity, the interface between the electrolyte and the electrodes was always another important factor that restricted the battery performance. Therefore, we use X-ray photoelectron spectroscopy (XPS) to investigate the chemical environment of the CPEs surface. N 1s spectra of PEO CPE and 30 H-Z-CPE were shown in Figure 3(a), the peak located at  $399.7\text{ eV}$  was attributed to the LiTFSI.<sup>[51-53]</sup> For the 30 H-Z-CPE, another peak located at  $402.0\text{ eV}$  was ascribed to the  $\text{N}^+.$ <sup>[54]</sup> It is worth noting that  $\text{N}^+$  does not belong to the dimethylimidazole ligand of ZIF-8 nor from the  $\text{TFSI}^-$  of LiTFSI, but from the [EMIM][TFSI] of the precursor of Li-IL. DFT calculation explained the interaction between  $\text{N}^+$  of EMIM $^+$  and N of hollow ZIF-8 made  $\text{Li}^+$  easy to combine with  $\text{TFSI}^-$  and improved the  $\text{Li}^+$  migration.<sup>[55]</sup> Therefore, the presence of a large amount of  $\text{N}^+$  in 30 H-Z-CPE



**Figure 3.** a) N 1s spectra of PEO CPE and 30 H-Z-CPE. b) F 1s spectra of PEO CPE and 30 H-Z-CPE. c) F 1s spectra of 30 H-Z-CPE before and after cycle. d) FT-IR spectra of PEO CPE and 30 H-Z-CPE. e) EIS plots of Li/PEO/Li and Li/30 H-Z-CPE/Li before cycle at  $60^{\circ}\text{C}$ . f) EIS plots of Li/30 H-Z-CPE/Li before and after cycle at  $60^{\circ}\text{C}$ .

indicates that the CPE contained more Li-IL, contributing to higher ionic conductivity. Meanwhile, F 1s spectra of the CPEs show two peaks in both the PEO CPE and the 30 H-Z-CPE, as shown in Figure 3(b). The peak located at 688.9 eV was attributed to LiTFSI and the other peak located at 685.0 eV was attributed to LiF.<sup>[56–58]</sup> LiF was derived from the decomposition of LiTFSI, which consumed a large amount of active Li<sup>+</sup>, resulting in the low conductivity of the CPEs. More importantly, excessive deposition of insulating LiF on the surface of the CPEs directly affects electrochemical cycling performance. Compared with PEO CPE, the LiF in 30 H-Z-CPE was greatly reduced, which indicates the hollow ZIF-8/IL filler could effectively inhibit the formation of LiF on the CPEs surface, thereby improving the cycling stability. The analysis above was consistent with the MD simulation of the Li-IL conduction mechanism in MOF nanopores, which illustrated the LiTFSI was formed due to the interaction of Li-IL and MOF to restrain anion-bunching.<sup>[59]</sup> Especially, as shown in Figure 3(c), compared to 30 H-Z-CPE before cycle, the content of LiF was essentially unchanged after cycle, which illustrated the novel core-shell structure filler could suppress the decomposition of LiTFSI to keep the stability of LiF on the interface between electrolyte and electrode.

In addition, Fourier-transform infrared (FT-IR) spectroscopy are used to obtain the surface chemical information of the thin-enough CPEs. Figure 3(d) shows the FT-IR spectra of the PEO CPE and 30 H-Z-CPE, and Table S1 lists the assignments of the peak positions in Figure 3(d). The peaks located at around 1064, 1144, 1193, and 1338 cm<sup>-1</sup> in PEO CPE and 30 H-Z-CPE were attributed to SNS stretch, SO<sub>2</sub> stretch, CF<sub>3</sub> stretch and SO<sub>2</sub> stretch, respectively. Compared with PEO CPE, the Li<sub>2</sub>CO<sub>3</sub> peaks located at near 875, 1457, 1510 cm<sup>-1</sup> in 30 H-Z-CPE disappeared completely, and the LiOH peak located at around 3676 cm<sup>-1</sup> sharply receded. Li<sub>2</sub>CO<sub>3</sub> and LiOH species were formed with H<sub>2</sub>O and CO<sub>2</sub> during the period of exposure to air in the time of CPEs preparation process and tremendously increased the interface resistance.<sup>[60]</sup> Therefore, hollow ZIF-8/IL filler can restrain the formation of Li<sub>2</sub>CO<sub>3</sub> and LiOH to improve the transmission of Li<sup>+</sup> at the interface. Furthermore, we measured interface impedance ( $R_i$ ) by EIS test to investigate the compatibility between electrolyte and electrode.<sup>[61,62]</sup> The  $R_i$  was immensely depended on the passive layer resistance ( $R_p$ ) corresponding to the interface between lithium and organic solvent in the CPE, while the charge transfer resistance ( $R_{ct}$ ) corresponding to the reaction of Li<sup>+</sup> + e → Li was negligible. As shown in Figure 3(e), compared to the  $R_i$  of 320 Ω for PEO, the  $R_i$  attributed to the 30 H-Z-CPE was greatly decreased to 149.6 Ω before cycle. Meanwhile, the  $R_i$  attributed to the 30 H-Z-CPE was 332.9 Ω after cycle, as shown in Figure 3(f), which was only slightly higher than the  $R_i$  attributed to PEO of 320 Ω before cycle, indicating that the hollow ZIF-8/IL significantly improved the interface compatibility between the anode and electrolyte.

Besides, we also use SEM and atomic force microscopy (AFM) to investigate the surfaces of the PEO CPE and the x H-Z-CPEs, which largely determines the interfacial contacts between the electrode and electrolyte. Figure 4(a–c) and Figure 4(d–f)

show the AFM height images in both 2D and 3D and SEM images of the CPEs with zero, 30%, and 50% fillers, respectively. Compared with the PEO CPE, the surface height variation of 30 H-Z-CPE ~89 nm was much lower than that of pure PEO CPE from ~2 μm as shown in Figure 4(a and b), which illustrates that the surface flatness for the CPE containing optimal hollow ZIF-8/IL content was significantly improved. However, Figure 4(c) shows the surface height variation of 50 H-Z-CPE ~209 nm, indicating that the addition of redundant fillers causes the surface flatness to be poor again. We also quantified their surface roughness with root mean square (RMS) roughness of a representative surface area of 30 μm × 30 μm as listed in Table S2. The RMS roughness value of PEO CPE, 30 H-Z-CPE and 50 H-Z-CPE were 322 nm, 19.6 and 22.5 nm, respectively, declaring that the optimal mass of hollow ZIF-8/IL also demonstrates a small surface roughness. These observations are in accordance with the corresponding SEM images of CPE surfaces as shown in Figure 4(d–f). In Figure 4(d), several cracks and folds were present on the surface of PEO CPE due to a favorable complexation between the PEO polymer and the LiTFSI salt used.<sup>[63]</sup> In contrast, Figure 4(e) reveals a smooth surface for the 30 H-Z-CPE, illustrating that a moderate amount of hollow ZIF-8/IL could have better interfacial contact with the electrodes. In addition, the top-view SEM images of CPEs with other content of fillers were also checked, as shown in Figure S1. With the increase of filler amount, the wrinkles and cracks on the CPEs surface were gradually decreased and disappeared, and the surface smoothness was greatly improved (Figure S1 a–f). However, when the hollow ZIF-8/IL filler mass increased to 40%, the CPE surface was inundated with the aggregated filler particles and became bumpy again when the filler content continued to increase to 50%. It is noted that the CPE surfaces gradually broke into fragments, as shown in Figure S1(g and h). Moreover, the cross-sectional SEM images of the CPEs were used to determine the thickness of the CPEs and the dispersion of the fillers. Figure 4(h) shows the thickness of the filminess PEO CPE prepared by the tape casting is 47.8 μm. The thickness of ultra-thin 30 H-Z-CPE was 41.6 μm and the hollow ZIF-8/IL fillers with rhomboid dodecahedron structure were uniformly dispersed in the electrolyte film, as shown in Figure 4(i and j), which was beneficial to enhance the Li<sup>+</sup> transmission.<sup>[64]</sup> After cycle, the thickness of 30 H-Z-CPE was 52.52 μm, which was only slightly thicker than that before cycle, as shown in Figure 4(g). Importantly, as shown in Figure 4(k), we found that the morphology of hollow ZIF-8/IL filler was maintained well, meanwhile, no possible agglomeration position of lithium dendrite was found, which indicated the new core-shell structure filler could effectively inhibit the formation of lithium dendrite. The homogeneity of the hollow ZIF-8/IL fillers in the CPEs is also confirmed by EDS mapping of characteristic elements C, O, N, F, S and Zn elements, which are uniform in the CPEs as shown in Figure S2. Specifically, the distribution of the Zn element (Figure S2 m), belonging to the ZIF-8 fillers in the PEO matrix illustrated the fillers were uniformly dispersed in the CPEs.

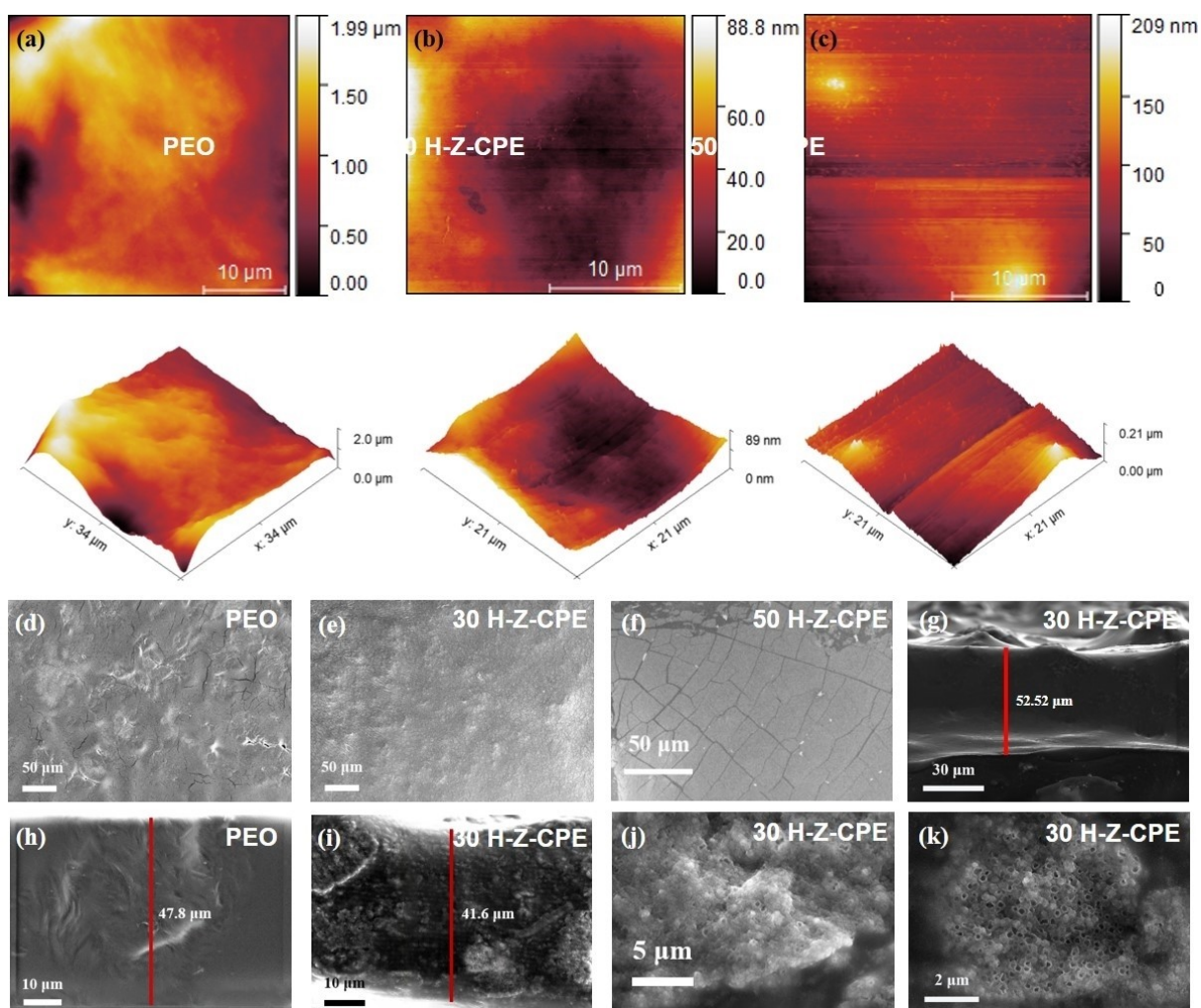


**Figure 4.** AFM and SEM images of a) and d) PEO CPE, b) and e) 30 H-Z-CPE and c) and f) 50 H-Z-CPE. Cross-sectional SEM images of h) PEO CPE, i) and j) 30 H-Z-CPE, g) and k) 30 H-Z-CPE after cycle.

### Electrochemical properties of CPEs and their battery performance

Figure 5(a) shows the ionic conductivities of the PEO CPE and  $x$ H-Z-CPEs at different temperatures to explore the temperature effect on the ionic conductivity. Although the 50 H-Z-CPE possessed the highest ionic conductivity at various temperatures, the poor surface flatness of the CPEs containing excessive fillers leads to poor interfacial contact thus failed in the later battery tests. It is noted that the ionic conductivity of 30 H-Z-CPE was  $1.41 \times 10^{-4} \text{ S cm}^{-1}$  at room temperature,  $7.46 \times 10^{-4} \text{ S cm}^{-1}$  at  $60^\circ\text{C}$  and there was no significant increase at even higher temperatures. Therefore, we focus on electrochemical performance tests of the 30 H-Z-CPE at  $60^\circ\text{C}$ . 30 H-Z-CPE has the highest ionic conductivity at various temperatures not only due to the amorphous phase transition caused by the addition of moderate fillers, but also due to the plasticization of sufficient IL.<sup>[65,66]</sup> The designed core-shell structure fillers with a cavity could accommodate and encapsulate a considerable amount of Li-IL. Meanwhile, the tape casting method solved the problem of excessive viscosity caused by adding adequate

IL to the CPE in the conventional casting method, which was difficult to strip off the film from the mold. Furthermore, the electrochemical stability window of the 30 H-Z-CPE was measured by linear sweep voltammetry (LSV) using a Li/30 H-Z-CPE/SS cell at  $60^\circ\text{C}$ . Figure 5(b) shows the electrochemical oxidation potential of the 30 H-Z-CPE is  $5.0 \text{ V vs. Li/Li}^+$ , which is significantly higher than that of PEO CPE ( $3.8 \text{ V vs. Li/Li}^+$ ) at  $60^\circ\text{C}$ , indicating that high-temperature operation of cell assembled by the CPE with an optimal filler is possible.<sup>[67]</sup> The relatively wide electrochemical window of the 30 H-Z-CPE illustrated the novel core-shell structure of hollow ZIF-8/IL filler was in favor of improving the tolerance to electrodes materials and made it possible to match well with high voltage cathode materials.<sup>[68]</sup> The lithium ion transference number ( $t_{\text{Li}}^+$ ) was an important factor affecting the electrochemical performance of the CPEs, and was measured combined with the chronoamperometry and EIS method and the result was calculated according to the formula Eq (S2).<sup>[69]</sup> The  $t_{\text{Li}}^+$  of the 30 H-Z-CPE was 0.41, which was much higher than the  $t_{\text{Li}}^+$  of 0.125 for PEO.<sup>[70]</sup> The great improvement of the new hollow ZIF-8/IL core-shell filler on the lithium ion migration number was attributed to the

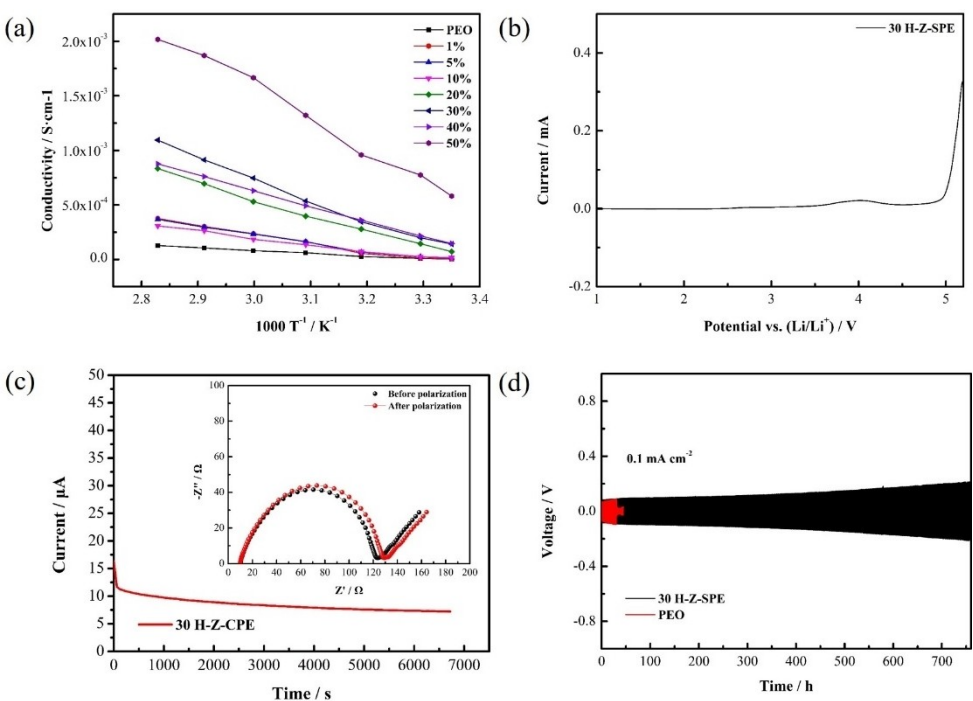


**Figure 5.** a) Temperature-dependent ionic conductivities of PEO CPE and x H-Z-CPE. b) LSV curves of PEO CPE and 30 H-Z-CPE at a scanning rate of 0.1 mV s<sup>-1</sup> at 60 °C. c) chronoamperometry curves and EIS plots of 30 H-Z-CPE at 60 °C. d) Voltage profiles of symmetric Li/PEO/Li and Li/30 H-Z-CPE/Li cells at a current density of 0.1 mA cm<sup>-2</sup> at 60 °C.

special Grotthuss-like conduction mechanism of lithium ion in the pores of ZIF-8 shell.<sup>[59]</sup> The interaction of ZIF-8 and Li-IL restrained the anion-bunching and lead Li<sup>+</sup> to follow the Grotthuss-like conduction mechanism with large mobility. On the above analysis, the galvanostatic charge-discharge tests were conducted by assembling the Li/CPE/Li symmetric batteries to evaluate the interfacial stability between CPEs and Li anode. As shown in Figure 5(d), the Li/PEO/Li and Li/30 H-Z-CPE/Li symmetric batteries operated at a current density of 0.1 mA cm<sup>-2</sup> under 60 °C and exhibited the disparate Li plating/stripping performance. For the Li/PEO/Li symmetric battery, the voltage pulsation was large, and the short circuit was occurred at only 60 h due to the rapid growth of lithium dendrites leading to the penetration of the electrode. In contrast, the Li/30 H-Z-CPE/Li symmetric battery owned an overpotential of merely approximately 0.05 V and could stable cycle 770 h without short-circuit. In addition, the symmetric cell fabricated by 30 H-Z-CPE also exhibited the excellent stability at higher current densities, as shown in Figure S3, which indicates the hollow ZIF-8/IL filler could effectively improve the interface contact between Li anode and CPE film, suppressed the formation of Li dendrites.

We rationalize the root cause for the inhibition of lithium dendrite by our designed core-shell structure filler as follows. First, the insulation of the shell layer of the hollow ZIF-8/IL filler effectively restrained the formation of lithium dendrites during the process of Li<sup>+</sup> transport. Secondly, the inner cavity of the hollow ZIF-8/IL fillers could not only provide space to store sufficient Li-IL but also offer low-potential electrons to deposit dead lithium.<sup>[71]</sup> Thirdly, the formed lithium dendrites were

difficult to penetrate the steady shell structure and coalesce into large pieces of dead lithium which caused the battery to short circuit.

Emphatically, the all-solid-state lithium metal batteries were assembled by NCM811 cathode, 30 H-Z-CPE composite polymer electrolyte, and Li metal anode in the CR2032 coin cells to measure the electrochemical performance. Although LiFePO<sub>4</sub> with better thermal stability is currently used as the cathode to assemble battery in the field of solid-state batteries, the energy density and theoretical capacity of the NCM811 cathode (300 Wh kg<sup>-1</sup>, 200 mAh g<sup>-1</sup>) far exceed that of LiFePO<sub>4</sub> cathode (160 Wh kg<sup>-1</sup>, 170 mAh g<sup>-1</sup>), which is more in line with the practical application prospect. As shown in Figure 6(a), all of the Li/30 H-Z-CPE/NCM811 full batteries could operate at 0.1 C under 60 °C but the cell assembled by the PEO CPE could not cycle under the same conditions due to the poor compatibility of PEO and NCM811 cathode.<sup>[72]</sup> The initial discharge capacity of the battery with the optimal hollow ZIF-8/IL fillers content was the highest capacity of 182.5 mAh g<sup>-1</sup>, comparing to the theoretical specific capacity of NCM811 (200 mAh g<sup>-1</sup>). The specific capacity of Li/30 H-Z-CPE/NCM811 cell decreased to 132.4 mAh g<sup>-1</sup> after 100 cycles with a capacity retention ratio of 73%. The Coulombic efficiency remained above 99% during the whole charge/discharge process. It is worth noting that the gram capacity of the Li/30 H-Z-CPE/NCM811 cell converted to actual areal capacity was 1.16–1.39 mAh cm<sup>-2</sup>, which was much higher than previous work. Figure 6(b) shows the typical galvanostatic charge and discharge curves of the Li/30 H-Z-CPE/NCM811 cell, which are carried out at a voltage of 2.8–4.3 V. The charge-discharge plateaus of the charge-discharge

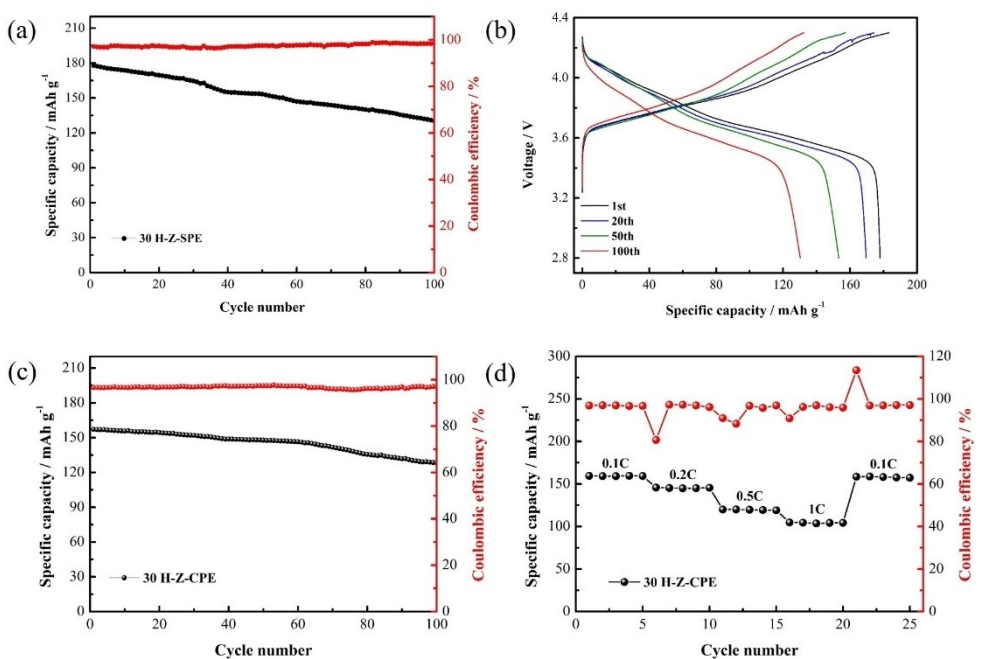


**Figure 6.** Electrochemical performances of the asymmetric cells, tested at 60 °C. a) Cycle performance of Li/30 H-Z-CPE/NCM811 cells at 0.1 C. b) Charge/discharge curves of the 1st, 20th, 50th and 100th cycles of cells using 30 H-Z-CPE at 0.1 C. c) Cycle performance of Li/30 H-Z-CPE/LiFePO<sub>4</sub> cells at 0.1 C. d) Rate performance at rates of 0.1–1 C.

curves of the cell were apparent at 0.1 C, which was quite similar to the lithium-NMC cells using a non-aqueous liquid electrolyte, indicating that the interfacial resistance between the electrodes and CPEs was kept small.<sup>[73]</sup> As a contrast, the electrochemical performances of Li/30 H-Z-CPE/LiFePO<sub>4</sub> cell was also measured, as shown in Figure 6(c). The initial discharge capacity of the battery using LiFePO<sub>4</sub> cathode was 157.2 mAh g<sup>-1</sup>, which was much lower than the 182.5 mAh g<sup>-1</sup> of battery using NCM811 cathode, but higher than the initial discharge capacity of Li/CPE/LiFePO<sub>4</sub> in most of analogous literatures for MOF/IL solid electrolyte, as shown in Table S3. In addition, Figure 6(d) exhibited the rate performance of cells using 30 H-Z-CPE at different current densities. The Li/30 H-Z-CPE/LiFePO<sub>4</sub> cell showed the high discharge capacity of 159.4, 145.7, 119.9, 104.7 mAh g<sup>-1</sup> at 0.1 C, 0.2 C, 0.5 C and 1 C, respectively. Especially, the recoverable capacity was nearly 100% of 158.5 mAh g<sup>-1</sup> when the current density switched to 0.1 C. As shown above, the CPEs with hollow ZIF-8/IL fillers show great rate performance and cycle stability benefit from its unique core-shell structure. The CPEs containing sufficient Li-IL prepared by the tape casting method greatly improve the interface contact by increasing interface wettability, which vastly broadens the practical application prospect of CPEs.

## Conclusion

In conclusion, thin ( $\approx$ 50  $\mu$ m) CPEs are successfully manufactured by novel tape casting method with hollow ZIF-8/IL filler into PEO substrates. The 30 H-Z-CPE shows high ionic conductivity of  $1.41 \times 10^{-4}$  Scm<sup>-1</sup> at 25 °C and  $7.46 \times 10^{-4}$  Scm<sup>-1</sup> at

60 °C due to the amorphization, favorable surface flatness and low roughness due to the uniform dispersion of fillers, good thermal stability due to the encapsulation of the Li-IL and wide electrochemical stability window (5.0 V). Notably, the Li symmetric cell assembled by 30 H-Z-CPE exhibits ability to withstand Li anode and cycles stably for 770 h. The Li/30 H-Z-CPE/NCM811 asymmetric cell exhibits a specific capacity of 182.5 mAh g<sup>-1</sup> and capacity retention of 73% after 100 cycles at 0.1 C and 60 °C. The unique hollow structure fillers formed by etching ZIF-8 can not only inhibit the penetration of lithium dendrite through the insulating shell, but also store enough Li-IL in the internal cavity to compensate for the lithium loss during the cycle, thus expanding the prospect for the development of a new generation of stable and efficient CPEs.

## Acknowledgements

The authors appreciate the support from the National Natural Science Foundation of China (Grant NO. 21873069).

## Conflict of Interest

The authors declare no conflict of interest.

**Keywords:** composite polymer electrolyte (CPE) · hollow ZIF-8 · interfacial contact · ionic liquid · Li-ion conductivity · lithium metal battery

- [1] J. M. Tarascon, M. Armand, *Nature* **2001**, *414*, 359–367.
- [2] Y. Tang, Y. Zhang, W. Li, B. Ma, X. Chen, *Chem. Soc. Rev.* **2015**, *44*, 5926–5940.
- [3] D. Lin, Y. Liu, Y. Cui, *Nat. Nanotechnol.* **2017**, *12*, 194–206.
- [4] J. B. Goodenough, K.-S. Park, *J. Am. Chem. Soc.* **2013**, *135*, 1167–1176.
- [5] R. Bouchet, S. Maria, R. Meziane, A. Aboulaich, L. Lienafa, J.-P. Bonnet, T. N. T. Phan, D. Bertin, D. Gigmes, D. Devaux, R. Denoyel, M. Armand, *Nat. Mater.* **2013**, *12*, 452–457.
- [6] J.-F. Wu, X. Guo, *J. Mater. Chem. A* **2019**, *7*, 2653–2659.
- [7] Z. Zhang, Y. Huang, H. Gao, J. Hang, C. Li, P. Liu, *J. Membr. Sci.* **2020**, *598*, 117800.
- [8] K. Xu, *Chem. Rev.* **2014**, *114*, 11503–11618.
- [9] E. Quartarone, P. Mustarelli, *Chem. Soc. Rev.* **2011**, *40*, 2525–2540.
- [10] D. Zhang, A. Dai, M. Wu, K. Shen, T. Xiao, G. Hou, J. Lu, Y. Tang, *ACS Energy Lett.* **2020**, *5*, 180–186.
- [11] W. Zhou, Z. Wang, Y. Pu, Y. Li, S. Xin, X. Li, J. Chen, J. B. Goodenough, *Adv. Mater.* **2019**, *31*, 1805574.
- [12] Y. Yuan, K. Amine, J. Lu, R. Shahbazian-Yassar, *Nat. Commun.* **2017**, *8*, 15806.
- [13] X. Yu, A. Manthiram, *Acc. Chem. Res.* **2017**, *50*, 2653–2660.
- [14] L. Long, S. Wang, M. Xiao, Y. Meng, *J. Mater. Chem. A* **2016**, *4*, 10038–10069.
- [15] K. Liu, R. Zhang, J. Sun, M. Wu, T. Zhao, *ACS Appl. Mater. Interfaces* **2019**, *11*, 46930–46937.
- [16] Q. Zhao, S. Stalin, C.-Z. Zhao, L. A. Archer, *Nat. Rev. Mater.* **2020**, *5*, 229–252.
- [17] G. Zhou, F. Li, H.-M. Cheng, *Energy Environ. Sci.* **2014**, *7*, 1307–1338.
- [18] D. R. MacFarlane, J. H. Huang, M. Forsyth, *Nature* **1999**, *402*, 792–794.
- [19] X. Yu, A. Manthiram, *Energy Storage Mater.* **2021**, *34*, 282–300.
- [20] W. Xiao, J. Wang, L. Fan, J. Zhang, X. Li, *Energy Storage Mater.* **2019**, *19*, 379–400.
- [21] L. Fan, X. Li, *Nano Energy* **2018**, *53*, 630–642.
- [22] D. Zhang, X. Xu, X. Huang, Z. Shi, Z. Wang, Z. Liu, R. Hu, J. Liu, M. Zhu, *J. Mater. Chem. A* **2020**, *8*, 18043–18054.
- [23] D. Zhang, X. Xu, S. Ji, Z. Wang, Z. Liu, J. Shen, R. Hu, J. Liu, M. Zhu, *ACS Appl. Mater. Interfaces* **2020**, *12*, 21586–21595.
- [24] D. Zhang, X. Xu, Y. Qin, S. Ji, Y. Huo, Z. Wang, Z. Liu, J. Shen, J. Liu, *Chem. Eur. J.* **2020**, *26*, 1720–1736.
- [25] Y. Li, D. Zhang, X. Xu, Z. Wang, Z. Liu, J. Shen, J. Liu, M. Zhu, *J. Energy Chem.* **2021**, *60*, 32–60.
- [26] F. Lv, Z. Wang, L. Shi, J. Zhu, K. Edstrom, J. Mindemark, S. Yuan, *J. Power Sources* **2019**, *441*, 227175.
- [27] Y. Li, G. He, S. Wang, S. Yu, F. Pan, H. Wu, Z. Jiang, *J. Mater. Chem. A* **2013**, *1*, 10058–10077.
- [28] Z. Wang, Z. Wang, L. Yang, H. Wang, Y. Song, L. Han, K. Yang, J. Hu, H. Chen, F. Pan, *Nano Energy* **2018**, *49*, 580–587.
- [29] Z. Sun, Y. Li, S. Zhang, L. Shi, H. Wu, H. Bu, S. Ding, *J. Mater. Chem. A* **2019**, *7*, 11069–11076.
- [30] X. Liu, R. Garcia-Mendez, A. R. Lupini, Y. Cheng, Z. D. Hood, F. Han, A. Sharafi, J. C. Idrobo, N. J. Dudney, C. Wang, C. Ma, J. Sakamoto, M. Chi, *Nat. Mater.* **2021**, *11*, 1485–1490.
- [31] S. Stegmaier, R. Schierholz, I. Povstugar, J. Barthel, S. P. Rittmeyer, S. Yu, S. Wengert, S. Rostami, H. Kungl, K. Reuter, R.-A. Eichel, C. Scheurer, *Adv. Energy Mater.* **2021**, *11*, 2100707.
- [32] B. Zheng, G. Maurin, *Angew. Chem. Int. Ed.* **2019**, *58*, 13734–13738; *Angew. Chem.* **2019**, *131*, 13872–13876.
- [33] K. Shen, L. Zhang, X. Chen, L. Liu, D. Zhang, Y. Han, J. Chen, J. Long, R. Luque, Y. Li, B. Chen, *Science* **2018**, *359*, 206–210.
- [34] Q. Yang, Q. Xu, S.-H. Yu, H.-L. Jiang, *Angew. Chem. Int. Ed.* **2016**, *55*, 3685–3689; *Angew. Chem.* **2016**, *128*, 3749–3753.
- [35] H. Zhu, X. Yang, E. D. Cranston, S. Zhu, *Adv. Mater.* **2016**, *28*, 7652.
- [36] Y. Du, J. Gao, L. Zhou, L. Ma, Y. He, X. Zheng, Z. Huang, Y. Jiang, *Adv. Sci.* **2019**, *6*, 1801684.
- [37] K. Jayaramulu, K. K. R. Datta, C. Roesler, M. Petr, M. Otyepka, R. Zboril, R. A. Fischer, *Angew. Chem. Int. Ed.* **2016**, *55*, 1178–1182; *Angew. Chem.* **2016**, *128*, 1193–1197.
- [38] B. Seoane, J. Coronas, I. Gascon, M. Etxeberria Benavides, O. Karvan, J. Caro, F. Kapteijn, J. Gascon, *Chem. Soc. Rev.* **2015**, *44*, 2421–2454.
- [39] X. Zhao, Y. Wang, D.-S. Li, X. Bu, P. Feng, *Adv. Mater.* **2018**, *30*, 1705189.
- [40] R. Zhao, Y. Wu, Z. Liang, L. Gao, W. Xia, Y. Zhao, R. Zou, *Energy Environ. Sci.* **2020**, *13*, 2386–2403.
- [41] Z. Wang, S. Wang, A. Wang, X. Liu, J. Chen, Q. Zeng, L. Zhang, W. Liu, L. Zhang, *J. Mater. Chem. A* **2018**, *6*, 17227–17234.
- [42] J. Zhang, Y. Bai, X.-G. Sun, Y. Li, B. Guo, J. Chen, G. M. Veith, D. K. Hensley, M. P. Paranthaman, J. B. Goodenough, S. Dai, *Nano Lett.* **2015**, *15*, 3398–3402.
- [43] S. Siyal, M. Li, H. Li, J.-L. Lan, Y. Yu, X. Yang, *Appl. Surf. Sci.* **2019**, *494*, 1119–1126.
- [44] C. Zhang, R. P. Lively, K. Zhang, J. R. Johnson, O. Karvan, W. J. Koros, *J. Phys. Chem. Lett.* **2012**, *3*, 2130–2134.
- [45] L. Zhu, P. Zhu, Q. Fang, M. Jing, X. Shen, L. Yang, *Electrochim. Acta* **2018**, *292*, 718–726.
- [46] C. Li, Y. Huang, X. Feng, Z. Zhang, P. Liu, *J. Membr. Sci.* **2019**, *587*, 11719.
- [47] J. Mindemark, B. Sun, E. Torma, D. Brandell, *J. Power Sources* **2015**, *298*, 166–170.
- [48] W. Kou, R. Lv, S. Zuo, Z. Yang, J. Huang, W. Wu, J. Wang, *J. Membr. Sci.* **2021**, *618*, 118702.
- [49] Z. Yang, Z. Sun, C. Liu, Y. Li, G. Zhou, S. Zuo, J. Wang, W. Wu, *J. Power Sources* **2021**, *484*, 229287.
- [50] M. Zeeshan, V. Nozari, S. Keskin, A. Uzun, *Ind. Eng. Chem. Res.* **2019**, *58*, 14124–14138.
- [51] Z. Zhang, Y. Huang, H. Gao, C. Li, J. Huang, P. Liu, *J. Membr. Sci.* **2021**, *621*, 118940.
- [52] H. Cheng, C. Zhu, M. Lu, Y. Yang, *J. Power Sources* **2007**, *173*, 531–537.
- [53] C. Xu, B. Sun, T. Gustafsson, K. Edstrom, D. Brandell, M. Hahlin, *J. Mater. Chem. A* **2014**, *2*, 7256–7264.
- [54] P. C. Howlett, N. Brack, A. F. Hollenkamp, M. Forsyth, D. R. MacFarlane, *J. Electrochem. Soc.* **2006**, *153*, A595–A606.
- [55] F. P. Kinik, C. Altintas, V. Balci, B. Koyuturk, A. Uzun, S. Keskin, *ACS Appl. Mater. Interfaces* **2016**, *8*, 30992–31005.
- [56] F. J. Simon, M. Hanauer, F. H. Richter, J. Janek, *ACS Appl. Mater. Interfaces* **2020**, *12*, 11713–11723.
- [57] F. J. Simon, M. Hanauer, A. Henss, F. H. Richter, J. Janek, *ACS Appl. Mater. Interfaces* **2019**, *11*, 42186–42196.
- [58] D. E. Mathew, S. Gopi, M. Kathiresan, A. M. Stephan, S. Thomas, *Electrochim. Acta* **2019**, *319*, 189–200.
- [59] M. Vazquez, M. Liu, Z. Zhang, A. Chandresh, A. B. Kanj, W. Wenzel, L. Heinke, *ACS Appl. Mater. Interfaces* **2021**, *13*, 21166–21174.
- [60] W. Feng, X. Dong, X. Zhang, Z. Lai, P. Li, C. Wang, Y. Wang, Y. Xia, *Angew. Chem. Int. Ed.* **2020**, *59*, 5346–5349; *Angew. Chem.* **2020**, *132*, 5384–5387.
- [61] A. Song, Y. Huang, X. Zhong, H. Cao, B. Liu, Y. Lin, M. Wang, X. Li, *J. Membr. Sci.* **2018**, *556*, 203–213.
- [62] S.-D. Gong, Y. Huang, H.-J. Cao, Y.-H. Lin, Y. Li, S.-H. Tang, M.-S. Wang, X. Li, *J. Power Sources* **2016**, *307*, 624–633.
- [63] S. Jayanthi, B. Sundaresan, *Ionics* **2015**, *21*, 705–717.
- [64] W. Zhang, J. Nie, F. Li, Z. L. Wang, C. Sun, *Nano Energy* **2018**, *45*, 413–419.
- [65] S. N. Banitala, D. Semnani, B. Rezaei, A. A. Ensafi, *Polym. Adv. Technol.* **2019**, *30*, 1234–1242.
- [66] K. Karuppasamy, H. W. Rhee, P. A. Reddy, D. Gupta, L. Mitu, A. R. Polu, X. S. Shajan, *J. Ind. Eng. Chem.* **2016**, *40*, 168–176.
- [67] J. Tan, X. Ao, A. Dai, Y. Yuan, H. Zhuo, H. Lu, L. Zhuang, Y. Ke, C. Su, X. Peng, B. Tian, J. Lu, *Energy Storage Mater.* **2020**, *33*, 173–180.
- [68] Z. Wang, R. Tan, H. Wang, L. Yang, J. Hu, H. Chen, F. Pan, *Adv. Mater.* **2018**, *30*, 1704436.
- [69] B. Liu, Y. Huang, H. Cao, L. Zhao, Y. Huang, A. Song, Y. Lin, X. Li, M. Wang, *J. Membr. Sci.* **2018**, *545*, 140–149.
- [70] W. Tang, S. Tang, C. Zhang, Q. Ma, Q. Xiang, Y.-W. Yang, J. Luo, *Adv. Energy Mater.* **2018**, *8*.
- [71] M. Huang, Z. Yao, Q. Yang, C. Li, *Angew. Chem. Int. Ed.* **2021**, *60*, 14040–14050.
- [72] S. Kaboli, H. Demers, A. Paolella, A. Darwiche, M. Dontigny, D. Clement, A. Guerfi, M. L. Trudeau, J. B. Goodenough, K. Zaghib, *Nano Lett.* **2020**, *20*, 1607–1613.
- [73] J. Li, W. Li, S. Wang, K. Jarvis, J. Yang, A. Manthiram, *Chem. Mater.* **2018**, *30*, 3101–3109.

Manuscript received: October 16, 2021

Revised manuscript received: November 23, 2021

Accepted manuscript online: December 14, 2021

Version of record online: December 27, 2021